Nanoscale

Accepted Manuscript

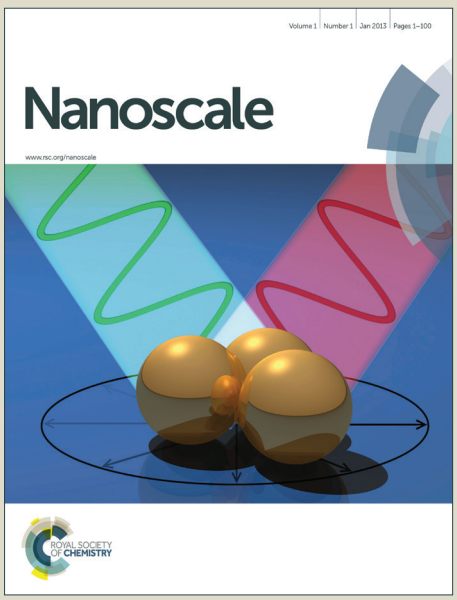

ROYAL SOCIETY OF CHEMISTRY

www.rsc.org/nanoscale

Large−area synthesis of monolayer $MoS_{2(1-x)}Se_{2x}$ with a tunable band gap and its enhanced electrochemical catalytic activity

Lei Yang[1,2], Qi Fu[1], Wenhui Wang[1], Jian Huang[1], Jianliu Huang[3], Jingyu Zhang[4], Bin Xiang[1,2*]

[1]Department of Materials Science & Engineering, CAS key Lab of Materials for Energy Conversion, University of Science and Technology of China, Hefei, Anhui, 230026, China

[2]Synergetic Innovation Center of Quantum Information & Quantum Physics, University of Science and Technology of China, Hefei, Anhui 230026, China

[3]Hefei National Laboratory for Physical Sciences at the Microscale, University of Science and Technology of China, Hefei, Anhui, 230026, China

[4]Molecular Foundry, Lawrence Berkeley National Laboratory, 1 Cyclotron Rd, Berkeley, CA 94720, USA

[*]Corresponding authors: binxiang@ustc.edu.cn

"Band gap engineering" in two-dimensional (2D) materials plays an important role in tailoring their physical and chemical properties. The tuning of the band gap is typically achieved by controlling the composition of the semiconductor alloys.[1-3] However, large-area preparation of 2D alloys remains a major challenge. Here, we report the large-area synthesis of high-quality monolayer $MoS_{2(1-x)}Se_{2x}$ with a size coverage of hundreds of microns using a chemical vapor deposition method. The photoluminescence (PL) spectroscopy results confirm the tunable band gap in $MoS_{2(1-x)}Se_{2x}$, which is modulated by varying the Se content. Atomic-scale analysis was performed and the chemical composition was characterized using high-resolution scanning transmission electron microscopy and X-ray photoemission spectroscopy. With the introduction of Se into monolayer MoS_2, it leads to enhanced catalytic activity in an electrochemical reaction for hydrogen generation, compared to monolayer MoS_2 and $MoSe_2$. It is promising as a potential alternative to expensive noble metals.

1 Introduction

Layered transition metal dichalcogenides (LTMDs) such as MoS_2 and $MoSe_2$ have attracted considerable attention because of their special properties in batteries,[4] gas sensors,[5] transistors[6,7] and catalysts.[8] Decreasing the layer number down to a monolayer triggers a transition from an indirect band gap to a direct band gap.[9,10] This novel property provides monolayer LTMDs with excellent potential for applications in optoelectronics and electronic devices.[7,11] To enhance the optoelectronic device performance, the achievement of a tunable band gap plays a key role. Substantial efforts have been made to modulate the band gap of 2D materials, like chemical doping,[12] ion intercalation,[13,14] the presence of biological species.[15] Recently, theoretical calculations and experimental investigations have demonstrated a tunable band gap for 2D semiconductor alloys.[1-3,16-19] Chen et al. reported that a tunable band gap can be achieved from 1.82 to 1.99 eV in a monolayer $Mo_{1-x}W_xS_2$ alloy cleaved from bulk crystals.[17] Chemical vapor deposition (CVD) or physical vapor deposition (PVD) have also been utilized to synthesize $MoS_{2(1-x)}Se_{2x}$ monolayer alloys with a tunable band gap by varying the S content.[1,2,19] Currently, the monolayer $MoS_{2(1-x)}Se_{2x}$ has been demonstrated with a size of ~ 50 μm achieved by using inorganic precursors in a CVD process.[1] The larger size of monolayer $MoS_{2(1-x)}Se_{2x}$ synthesis has also been reported by using organic precursors in a CVD process.[19] However, the organic precursors generally cause a carbonaceous layer staying on the surface of the as-grown monolayer,[19] which could modify the electrical and optical properties of monolayer $MoS_{2(1-x)}Se_{2x}$. For real applications of monolayer LTMDs in transistors, large-scale synthesis and the clean surface would make monolayer LTMD-based integrated digital and analog circuit fabrications feasible.[20] In this paper, we report the large-area synthesis of high-quality monolayer $MoS_{2(1-x)}Se_{2x}$ with several-hundred-micrometer size coverage using a CVD method. Optical microscopy (OM), atomic force microscopy (AFM),

Raman spectroscopy and X-ray photoemission spectroscopy (XPS) were utilized to characterize the as-grown large area monolayer $MoS_{2(1-x)}Se_{2x}$. PL measurements were employed to demonstrate the band structure of $MoS_{2(1-x)}Se_{2x}$ with a tunable band gap of ~300 meV. Atomic scale analysis of the monolayer $MoS_{2(1-x)}Se_{2x}$ was conducted using high-resolution scanning transmission electron microscopy (HRSTEM). The electrochemical catalytic activity of the as-grown monolayer $MoS_{2(1-x)}Se_{2x}$ was also demonstrated in the hydrogen evolution reaction (HER).

2 Results and Discussion

Monolayer $MoS_{2(1-x)}Se_{2x}$ alloys were synthesized on a SiO_2/Si substrate at atmospheric pressure using a CVD method (details in Methods). Fig. 1a presents a schematic illustration of the single-zone tube furnace employed for the growth of the monolayer $MoS_{2(1-x)}Se_{2x}$ alloys. S and Se powders were placed in the upstream side of the MoO_3 powder loaded in the middle of the tube furnace. During the growth, a mixture of argon-hydrogen (5%) gas with 50sccm was utilized as the carrier and reduction gas. As we know, hydrogen is more reductive than sulfur and the chemical reactivity of Se is much lower than that of S. With the introduction of H_2, the reduction of MoO_3 to MoO_{3-x} becomes much easier, which facilitates the further reactions. However, the growth of transition metal dichalcogenides can be restrained if the concentration of hydrogen gas is too high.[21] Therefore, with the consideration of both reaction kinetics and size control, we chose 5% hydrogen gas mixed with argon gas for the synthesis. Fig. 1b presents a representative OM image of the as-synthesized monolayer $MoS_{1.22}Se_{0.78}$ alloy, which shows the hundreds of microns size of the monolayer. Fig. 1c is the corresponding high magnification OM images of the as-grown monolayer $MoS_{1.22}Se_{0.78}$. The optical images of monolayer $MoS_{2(1-x)}Se_{2x}$ with different Se content are shown in Fig. S1. The thickness of the as-grown monolayer $MoS_{1.22}Se_{0.78}$ was characterized by AFM (Fig. 1d). The height profile in the inset of Fig. 1d indicates that the measured thickness was ~ 0.71 nm,

which is consistent with the previously reported value.[2]

Raman spectroscopy was utilized to characterize the phonon vibration mode properties of the as-grown $MoS_{2(1-x)}Se_{2x}$. Fig. 2a presents the Raman spectra of the as-synthesized monolayer $MoS_{2(1-x)}Se_{2x}$ (x=0, 0.11, 0.39, 0.51, 0.61, 1). There are two sets of peaks in the Raman spectra, which are corresponding to MoS_2 representative feature (~ 400 cm^{-1}) and $MoSe_2$ typical feature (~ 240 cm^{-1}), respectively. By increasing the Se content in the monolayer $MoS_{2(1-x)}Se_{2x}$, the MoS_2-like E^1_{2g} and A_{1g} modes shift to low frequency. Monolayer MoS_2 consists of three identical sub-layers, one layer of Mo atoms sandwiched by two planes of sulfur atoms.[22] The Mo atoms are bonded with six S atoms forming Mo-S bonds symmetrically. Three Mo-S bonds are above the Mo atoms plane, and three Mo-S bonds are below the Mo atoms plane (Fig. S2a).[23] As the Se atoms substitute for part of the S sites, the original MoS_2 crystal symmetry is broken because of the local distortion from the introduction of the Se atoms with larger atomic radius.[24] This distortion changes the bond length of the original Mo-S and Mo-Mo bonds. Therefore, an external tensile strain is exerted on the original MoS_2 lattices, which softens the atomic vibrations of the E^1_{2g} and A_{1g} modes of MoS_2.[25] By increasing the Se content in the monolayer $MoS_{2(1-x)}Se_{2x}$, the tensile strain increases, leading to the red shifts in the E^1_{2g} and A_{1g} vibration modes. In the monolayer $MoSe_2$, the E^1_{2g} and A_{1g} mode are located at 286cm^{-1} and 240cm^{-1}. With the introduction of Se in the monolayer $MoS_{2(1-x)}Se_{2x}$, the $MoSe_2$ like E^1_{2g} and A_{1g} modes emerge and become more and more predominant, which agrees with the reported result.[26]

Fig. 2b demonstrates that the PL peak feature in the monolayer $MoS_{2(1-x)}Se_{2x}$ shifts toward longer wavelength with an increase of the Se content. The correlation of the band gap as a function of the Se content is demonstrated in Fig. 2c by extracting the PL peak locations from Fig. 2b. The increase of Se content reduces the band gap in the monolayer $MoS_{2(1-x)}Se_{2x}$, in agreement with our

theoretical calculations as shown in Fig. 2c (details in Methods). According to the molecular orbital theory, most features of MX_2 (M= Mo, W; X=S, Se) are associated with the non-bonding *d* bands, which are located within the gap between the bonding (σ) and anti-bonding (σ *) bands of M–X bonds (Fig. S2, Supporting Information).[27-29] The formation of the *d* bands is dominated by several factors, such as the crystal structure and inter-nucleus distances of M-X, M-M, and X-X.[28] For the 2H MoX_2 (X=S, Se), the non-bonding *d* bands are mainly derived from the Mo-d_z^2, Mo-$d_{x^2-y^2, xy}$ and Mo-$d_{xz,yz}$ orbitals. The $d_{x^2-y^2, xy}$ and $d_{xz, yz}$ orbitals are generally empty, and the Mo-d_z^2 orbitals are fully occupied. The gap between the Mo-d_z^2 and Mo-$d_{x^2-y^2,xy}$ orbitals corresponds to the band gap of 2H MoX_2.[27-29] The Mo atoms and S atoms are coordinated through ionic-covalent interactions with electronegativity values of 1.6 and 2.5, respectively.[10,30] Compared with the S atom, the Se atom has a relative smaller electronegativity value of 2.4.[30] With the introduction of Se atoms into the MoS_2 crystals, the non-bonding *d* bands broaden resulting from the stronger covalent effects in $MoS_{2(1-x)}Se_{2x}$.[27,31] Therefore, the non-bonding *d* bands broaden in the structure of monolayer $MoS_{2(1-x)}Se_{2x}$, leading to a smaller band gap.[27,31] The stronger tensile strain induced by the substitution of Se atoms for the S sites could also contribute to the reduction of the band gap in monolayer $MoS_{2(1-x)}Se_{2x}$.[25] Noting that the calculated band gap values are smaller than that of experimental data measured from the PL spectra. We attribute it to the standard exchange-correlation functions of the generalized gradient approximation (GGA) used in the calculations, which causes the band gap energy reduced.[32] XPS was used to examine the chemical states and the Se content in the as-synthesized monolayer $MoS_{2(1-x)}Se_{2x}$ (details in experimental section). Fig. 3a-c present the detailed XPS scans for the Mo, S and Se binding energies in the as-grown monolayer $MoS_{2(1-x)}Se_{2x}$ (x=0, 0.11, 0.39, 0.51, 0.61, 1). The binding energies of Mo $3d_{5/2}$ and Mo $3d_{3/2}$ are observed at 229.6 and 232.8 eV, similar to the reported values for MoS_2 or

$MoSe_2$.[33,34] The peaks at 162.7 and 163.9 eV in Fig. 3b are attributed to S 2 $p_{3/2}$ and S $2p_{1/2}$ binding energies, respectively.[2,35] In Fig. 3c, the Se peaks at 54.9 and 55.7 eV are indexed to be Se $3d_{5/2}$ and Se $3d_{3/2}$, respectively. With increasing the Se content in the monolayer $MoS_{2(1-x)}Se_{2x}$, the Se $3p_{3/2}$ peak appears and becomes stronger, while the intensity of S $2p_{1/2}$ and S $2p_{3/2}$ peaks decreases. These results are consistent with previously reported values.[2,33,35]

HRSTEM was employed to image the distribution of the S and Se atoms in the monolayer $MoS_{2(1-x)}Se_{2x}$. Fig. 4a presents a morphology image of the as-synthesized monolayer $MoS_{1.22}Se_{0.78}$ that was transferred to the Cu TEM grid with the aid of a poly (methyl methacrylate) (PMMA) solution (details in Methods). Fig. 4b presents a HRSTEM image of the basal plane of the as-synthesized monolayer $MoS_{1.22}Se_{0.78}$ alloy. The Mo sites and bi-chalcogen (X_2) sites can be easily distinguished, as denoted by the hexagonal rings of alternative molybdenum and sulfur color cartoon spheres in each unit. In the HRSTEM imaging, the brightness of the atom is proportional to the mean square atom numbers of ($\overline{Z^2}$) along the direction of the electron beam.[36] As observed in Fig. 4b, all the Mo sites have similar brightness and are brighter than most of the X_2 sites. The atomic number of Se is 34, which is larger than that of S which is 16. As long as two Se atoms replace S-S sites, the brightness in the HRSTEM image becomes brighter than that of the original S-S sites. As one of the S-S sites is replaced by a single Se atom, the S-Se sites become brighter than the S-S sites but less bright than the Se-Se sites, as denoted by the purple and orange cycles in Fig. 4b, respectively. Fig. 4c is the magnification of Fig. 4b. The intensity profile in Fig. 4d corresponds to the brightness of atoms in Fig. 4c, as denoted by the yellow line. The brightness becomes increasingly bright from left to right, which corresponds to the S-S, S-Se and Se-Se sites, respectively.

To assess the catalytic activity of the as-grown $MoS_{2(1-x)}Se_{2x}$, electrochemical measurements

in a HER were performed in a 0.5 M H_2SO_4 solution with a three-electrode cell on glassy carbon electrodes (GCEs) (details in Methods). Monolayer $MoS_{2(1-x)}Se_{2x}$ was transferred to the GCE with the aid of PMMA solution (details in Methods). To remove the contaminants on the surface of the GCE, the electrode was cycled several times before any measurements. Fig. 5a presents a schematic illustration of the HER catalytic activity of monolayer $MoS_{2(1-x)}Se_{2x.}$ The electrons are transported from the GCE to the monolayer $MoS_{2(1-x)}Se_{2x}$ and are eventually trapped by the hydrogen ions. All the potentials were calibrated to a reversible hydrogen electrode (RHE). The polarization curves of the catalytic activity for monolayer $MoS_{2(1-x)}Se_{2x}$ (x=0, 0.39, 0.51, 0.61, 1) are presented in Fig. 5b. The glassy carbon is catalytically inactive for the HER, which is confirmed by the polarization curve of the blank GCE in Fig. 5b. The onset potentials are 300 mV, 273 mV and 279 mV at the current density of 10 mA/cm^2 in the $MoS_{2(1-x)}Se_{2x}$ (x=0.39, 0.51, 0.61), respectively, which are smaller than that of MoS_2 (335 mV) and $MoSe_2$ (303 mV). The catalytic current densities in the $MoS_{2(1-x)}Se_{2x}$ (x=0.39, 0.51, 0.61) are larger than that of MoS_2 and $MoSe_2$ at a constant overpotential (The current density at the same potential in our monolayer MoS_2 is similar to the reported value of monolayer MoS_2[37]). It indicates that the ternary alloys exhibit the enhanced HER catalytic activities compared to the MoS_2 and $MoSe_2$. The Tafel slope is a typical parameter that is utilized to evaluate the electrocatalytic activity of the HER. Fig. 5c shows the Tafel slope of the monolayer $MoS_{2(1-x)}Se_{2x}$. The $MoS_{2(1-x)}Se_{2x}$ (x=0.39, 0.51, 0.61) exhibits the lower Tafel slope (100 mV/dec, 119 mV/dec, 106 mV/dec, respectively) than that of monolayer $MoSe_2$ (134 mV/dec) and MoS_2 (134 mV/dec). Another important parameter to evaluate the catalyst is the electrochemical stability. To investigate the stability of the monolayer $MoS_{2(1-x)}Se_{2x}$, we determined the HER activities of the monolayer $MoS_{2(1-x)}Se_{2x}$ (x=0.61) at a constant potential of -0.24 V for 22 h. Upon monitoring the process, only slight degradation of the current density was observed, as

demonstrated in Fig. 5d. This slight degradation may be due to H_2 bubbles remaining on the surface, which suppresses the subsequent reaction.[38]

In general, the basal plane of MX_2 (M=Mo, W; X=S, Se) is catalytically inert, whereas the surface edges as active centers exhibit catalytic activities.[39,40] The localized edge sites, such as the unsaturated sulfur atoms on the surface, play a key role in the enhanced catalytic performance of the HER.[41] Fig. 1d reveals the zigzag features at the perimeter of the as-grown monolayer $MoS_{2(1-x)}Se_{2x}$, which suggests high-index surface planes with a high density of edge sites exposed on the surface. These edge sites are responsible for the high catalytic performance of monolayer $MoS_{2(1-x)}Se_{2x}$ in the HER.[42,43] Theoretical calculations indicated that the free energy of hydrogen adsorption plays a key role in its HER.[39] The hydrogen adsorption energy on the active edge sites is too weak for MoS_2 (ΔG_H = 80 meV)[39,40] but is too strong for $MoSe_2$ (ΔG_H = -140 meV).[44] Too strong hydrogen adsorption energy leads to permanent blocking of the catalytic surface while too weak energy causes the adsorbate residence time too short for bond breaking.[45] With the introduction of Se into monolayer MoS_2, a proper hydrogen adsorption energy can be achieved. As a result, improved HER catalytic activities are achieved in the $MoS_{2(1-x)}Se_{2x}$ (x=0.39, 0.51, 0.61), compared to monolayer MoS_2 and $MoSe_2$. Noting that the catalytic current density of $MoS_{2(1-x)}Se_{2x}$ (x= 0.61) is larger than that of x=0.51 and x=0.39, which may be caused by an improved electrical conductivity of x=0.61 with a narrower band gap.[26] The highly active catalysis with stable performance makes monolayer $MoS_{2(1-x)}Se_{2x}$ a potential candidate to replace expensive noble metals for HER applications.

3 Conclusions

The preparation of large-area 2D material alloys still remains challenging. We reported a large-area synthesis technique for high-quality monolayer $MoS_{2(1-x)}Se_{2x}$ alloys of hundreds of microns in size using a CVD method. The tunable band gap of the alloys was demonstrated by

controlling the Se content, which was confirmed by PL spectroscopy. Atomic-scale analysis revealed that defect-free single crystalline monolayer $MoS_{2(1-x)}Se_{2x}$ was prepared using this approach. Monolayer $MoS_{2(1-x)}Se_{2x}$ with different Se content shows different HER catalytic activities. $MoS_{2(1-x)}Se_{2x}$ (x=0.39, 0.51, 0.61) exhibits higher catalytic activity, compared with monolayer MoS_2 and $MoSe_2$. It was explained by the fact that proper hydrogen adsorption energy is achieved by the introduction of Se into MoS_2. Our growth parameters could be used as a general guideline for the large-area synthesis of other 2D alloys.

4 Experimental Section

Synthesis of monolayer $MoS_{2(1-x)}Se_{2x}$ (x=0.11, 0.39, 0.51, 0.61) alloy: Monolayer $MoS_{2(1-x)}Se_{2x}$ (x=0.11, 0.39, 0.51, 0.61) was grown on a SiO_2 (300 nm)/Si substrate in a homemade quartz tube furnace using an atmospheric pressure CVD (APCVD) method. Before growth, SiO_2/Si substrates were sequentially cleaned using sonication in acetone, absolute ethanol and distilled water for 20 minutes each. The ceramic boat loaded with 30 mg MoO_3 powder was placed at the center of the quartz tube, and the cleaned substrates were placed facedown above the boat. Another two ceramic boats filled with sulfur powder and selenium powder were located in the upstream of the tube at distances of 12 cm and 8 cm from the center of the tube, respectively. Before heating the furnace, we purged the system with a mixture of argon-hydrogen (5%) gas for 20 min to exhaust the air. Then, the furnace was maintained at 655°C for 5 min at a heating rate of 15°C/min with a 50 sccm argon-hydrogen (5%) mixture gas as the carrier gas and reduction gas. After the furnace was naturally cooled to room temperature, monolayer $MoS_{2(1-x)}Se_{2x}$ (x=0.11, 0.39, 0.51, 0.61) alloys coated the substrates. The Se content in the monolayer $MoS_{2(1-x)}Se_{2x}$ alloy was modified by adjusting the weight of the S and Se powders.

Synthesis of monolayer MoS_2 and $MoSe_2$: The monolayer MoS_2 growth process is very similar to the procedure of synthesis of monolayer $MoS_{2(1-x)}Se_{2x}$ (x=0.11, 0.39, 0.51, 0.61) alloy by loading the sulfur powder at the upstream side with a 12 cm distance to the center of the tube. Regarding the growth of monolayer $MoSe_2$, the only difference in the growth parameters is that the monolayer $MoSe_2$ was grown at 750°C for 20 min by loading the selenium powder at the upstream side with a 10.5 cm distance to the center of the tube.

Theoretical calculation method: We simulated the band gap of monolayer $MoS_{2(1-x)}Se_{2x}$ using CASTEP, a package for the density functional theory (DFT) calculation. We selected the

ultrasoft pseudopotentials and used the Perdew-Burke-Ernzerhof (PBE) form of generalized gradient approximation (GGA) as electron exchange-correlation potential. Plane wave functions were used at a cutoff energy of 500 eV. We optimized the geometry by relaxed the ions until the maximum forces were less than 0.05 eV/Å and the total energy was converged to 5×10^{-5} eV/atom.

The quantitative analysis of the ratio of S and Se by XPS:

The ratio of S and Se can be calculated from the XPS results by the following formula:[35]

$$S/Se = (I_S * F_{Se}) / (I_{Se} * F_S)$$

where I_S and I_{Se} are the areas under the peaks of S-$2p_{3/2}$ and Se-$3p_{3/2}$, respectively; F_S and F_{Se} represent the relative symmetric factors (R.S.F) for S-$2p_{3/2}$ (0.4453) and Se-$3p_{3/2}$ (0.8493) respectively.

TEM sample preparation: For the TEM observations, we transferred our as-grown monolayer $MoS_{2(1-x)}Se_{2x}$ onto Cu TEM grids. First, we spin-coated a PMMA layer onto the top of the monolayer $MoS_{2(1-x)}Se_{2x}$ on a SiO_2/Si substrate at 3000 rpm for 30 s. After baking the substrate at 100°C for 10 min, it was immersed into a 5 M KOH solution. The KOH solution etched the SiO_2 layer, causing the PMMA-caped monolayer $MoS_{2(1-x)}Se_{2x}$ to float on its surface. To remove the etchant and residues, we transferred the PMMA-caped monolayer $MoS_{2(1-x)}Se_{2x}$ to the deionized water and washed the caped monolayer several times. Finally, the PMMA-caped $MoS_{2(1-x)}Se_{2x}$ was scooped onto a Cu TEM grid, and the PMMA was dissolved with acetone droplets.

Transfer of as-grown monolayer $MoS_{2(1-x)}Se_{2x}$ onto GCE: We transferred our as-grown monolayer $MoS_{2(1-x)}Se_{2x}$ onto GCE using the PMMA-solution-based method. The process is illustrated in Fig. S3 in the supplemental information and is similar to the procedure described under TEM sample preparation.

Electrocatalytic measurements: The electrochemical experiment was performed in a three-electrode cell with an electrochemical workstation. A three-electrode configuration using a naked glass carbon electrode (GCE, d = 3 mm) adhered with monolayer $MoS_{2(1-x)}Se_{2x}$ as the working electrode, a Ag/AgCl (3 M KCl) electrode as the reference electrode and Pt wire as the counter electrode. All the results were iR-corrected in the paper, and all the potentials were vs. reversible hydrogen electrode (RHE). Linear sweep voltamperometry with a scan rate of 5 mV/s was conducted from 0.2 to -0.75 V vs. RHE for the polarization curve in 0.5 M H_2SO_4. The monolayer $MoS_{2(1-x)}Se_{2x}$ was transferred to the naked glass carbon electrode with the aid of the poly (methylmethacrylate) (PMMA) solution, as illustrated above. The HER tests based on the naked GCE were used as a control.

References

1 Q. Feng, Y. Zhu, J. Hong, M. Zhang, W. Duan, N. Mao, J. Wu, H. Xu, F. Dong, F. Lin, C. Jin, C. Wang, J. Zhang and L. Xie, *Adv. Mater.*, 2014, **26**, 2648–2653.

2 Y. Gong, Z. Liu, A. R. Lupini, G. Shi, J. Lin, S. Najmaei, Z. Lin, A. L. Elías, A. Berkdemir, G. You, H. Terrones, M. Terrones, R. Vajtai, S. T. Pantelides, S. J. Pennycook, J. Lou, W. Zhou and P. M. Ajayan, *Nano Lett.*, 2014, **14**, 442–449.

3 H.-P. Komsa and A. V. Krasheninnikov, *J. Phys. Chem. Lett.*, 2012, **3**, 3652–3656.

4 X. Cao, Y. Shi, W. Shi, X. Rui, Q. Yan, J. Kong and H. Zhang, *small*, 2013, **9**, 3433–3438.

5 D. J. Late, Y.-K. Huang, B. Liu, J. Acharya, S. N. Shirodkar, J. Luo, A. Yan, D. Charles, U. V. Waghmare, V. P. Dravid and C. N. R. Rao, *ACS Nano*, 2013, **7**, 4879–4891.

6 B. Radisavljevic, A. Radenovic, J. Brivio, V. Giacometti and A. Kis, *Nat. Nanotechnol.*, 2011, **6**, 147–150.

7 D. J. Late, B. Liu, H. S. S. R. Matte, V. P. Dravid and C. N. R. Rao, *ACS Nano*, 2012, **6**, 5635–5641.

8 J. Chen, X.-J. Wu, L. Yin, B. Li, X. Hong, Z. Fan, B. Chen, C. Xue and H. Zhang, *Angew. Chem.*, 2015, **127**, 1226–1230.

9 K. K. Kam and B. A. Parklnson, *J. Phys. Chem.*, 1982, **86**, 463–467.

10 K. F. Mak, C. Lee, J. Hone, J. Shan and T. F. Heinz, *Phys. Rev. Lett.*, 2010, **105**, DOI: 10.1103/PhysRevLett.105.136805.

11 O. Lopez-Sanchez, D. Lembke, M. Kayci, A. Radenovic and A. Kis, *Nat. Nanotechnol.*, 2013, **8**, 497–501.

12 S. Mouri, Y. Miyauchi and K. Matsuda, *Nano Lett.*, 2013, **13**, 5944–5948.

13 Y. Wang, J. Z. Ou, S. Balendhran, A. F. Chrimes, M. Mortazavi, D. D. Yao, M. R. Field, K. Latham, V. Bansal, J. R. Friend, S. Zhuiykov, N. V. Medhekar, M. S. Strano and K. Kalantar-zadeh, *ACS Nano*, 2013, **7**, 10083–10093.

14 Y. Wang, J. Z. Ou, A. F. Chrimes, B. J. Carey, T. Daeneke, M. M. Y. A. Alsaif, M. Mortazavi, S. Zhuiykov, N. Medhekar, M. Bhaskaran, J. R. Friend, M. S. Strano and K. Kalantar-zadeh, *Nano Lett.*, 2015, **15**, 883–890.

15 J. Z. Ou, A. F. Chrimes, Y. Wang, S. Tang, M. S. Strano and K. Kalantar-zadeh, *Nano Lett.*, 2014, **14**, 857–863.

16 K.-T. Lam, Y. Lu, Y. P. Feng and G. Liang, *Appl. Phys. Lett.*, 2011, **98**, DOI: 10.1063/1.3535604.

17 Y. Chen, J. Xi, D. O. Dumcenco, Z. Liu, K. Suenaga, D. Wang, Z. Shuai, Y.-S. Huang and L. Xie, *ACS Nano*, 2013, **7**, 4610–4616.

18 H. Li, X. Duan, X. Wu, X. Zhuang, H. Zhou, Q. Zhang, X. Zhu, W. Hu, P. Ren, P. Guo, L. Ma, X. Fan, X. Wang, J. Xu, A. Pan and X. Duan, *J. Am. Chem. Soc.*, 2014, **136**, 3756–3759.

19 J. Mann, Q. Ma, P. M. Odenthal, M. Isarraraz, D. Le, E. Preciado, D. Barroso, K. Yamaguchi, G. S. Palacio, A. Nguyen, T. Tran, M. Wurch, A. Nguyen, V. Klee, S. Bobek, D. Sun, T. F. Heinz, T. S. Rahman, R. Kawakami and L. Bartels, *Adv. Mater.*, 2014, **26**, 1399–1404.

20 L. Yu, Y.-H. Lee, X. Ling, E. J. G. Santos, Y. C. Shin, Y. Lin, M. Dubey, E. Kaxiras, J. Kong, H. Wang and T. Palacios, *Nano Lett.*, 2014, **14**, 3055–3063.

21 Y. Zhang, Y. Zhang, Q. Ji, J. Ju, H. Yuan, J. Shi, T. Gao, D. Ma, M. Liu, Y. Chen, X. Song, H. Hwang, Y. Cui and Z. Liu, *ACS Nano*, 2013, **7**, 8963–8971.

22 P. N. Ghosh and C. R. Maiti, *Phy. Rev. B*, 1983, **28**, 2237–2239.

23 T. Li, *Phys Rev. B*, 2012, **85**, DOI: 10.1103/PhysRevB.85.235407.

24 S. Horzum, H. Sahin, S. Cahangirov, P. Cudazzo, A. Rubio, T. Serin and F. M. Peeters, *Phys. Rev. B*, 2013, **87**, DOI: 10.1103/PhysRevB.87.125415.

25 A. Castellanos-Gomez, R. Roldán, E. Cappelluti, M. Buscema, F. Guinea, H. S. J. Zant and G. A. Steele, *Nano Lett.*, 2013, **13**, 5361–5366.

26 Q. Gong, L. Cheng, C. Liu, M. Zhang, Q. Feng, H. Ye, M. Zeng, L. Xie, Z. Liu and Y. Li, *ACS Catal.*, 2015, **5**, 2213–2219.

27 M. Chhowalla, H. S. Shin, G. Eda, L.-J. Li, K. P. Loh and H. Zhang, *Nat. Chem.*, 2013, **5**, 263–275.

28 J. A. Wilson and A. D. Yoffe, *Adv. Phys.*, 1969, **18**, 193–335.

29A. D. Yoffe, *Chem. Soc. Rev.*, 1976, **5**, 51–78.

30 W. Gordy and W. J. O. Thomas, *J. Chem. Phys.*, 1956, **24**, 439–444.

31 A. R. Beal and H. P. Hughes, *J. Phys. C: Solid State Phys.*, 1979, **12**, 881–890.

32 S. Lebègue and O. Eriksson, *Phy. Rev. B*, 2009, **79**, DOI:10.1103/PhyRevB.79.115409.

33 Y.-H. Chang, W. Zhang, Y. Zhu, Y. Han, J. Pu, J.-K. Chang, W.-T. Hsu, J.-K. Huang, C.-L.Hsu, M.-H. Chiu, T. Takenobu, H. Li, C.-I Wu, W.-H. Chang, A. T. S. Wee and L.-J. Li, *ACS Nano*, 2014, **8**, 8582–8590.

34 Y.-C. Lin, W. Zhang, J.-K. Huang, K.-K. Liu, Y.-H. Lee, C.-T. Liang, C.-W. Chu and L.-J. Li, *Nanoscale*, 2012, **4**, 6637–6641.

35 V. Kiran, D. Mukherjee, R. N. Jenjeti and S. Sampath, *Nanoscale*, 2014, **6**, 12856–12863.

36 S. J. Pennycook, in *Progress in Transmission Electron Microscopy*, ed. X.-F. Zhang and Z. Zhang, Tsinghua University Press, Beijing, 1999, Vol. I, P. 97.

37 J. Shi, D. Ma, G.-F. Han, Y. Zhang, Q. Ji, T. Gao, J. Sun, X. Song, C. Li, Y. Zhang, X.-Y. Lang, Y. Zhang and Z. Liu, *ACS Nano*, 2014, **8**, 10196–10204.

38 J. Xie, H. Zhang, S. Li, R. Wang, X. Sun, M. Zhou, J. Zhou, X. W. Lou (David) and Y.Xie, *Adv. Mater.*, 2013, **25**, 5807–5813.

39 B. Hinnemann, P. G. Moses, J. Bonde, K. P. Jørgensen, J. H. Nielsen, S. Horch, I. Chorkendorff and J. K. Nørskov, *J. Am. Chem. Soc.*, 2005, **127**, 5308–5309.

40 T. F. Jaramillo, K. P. Jørgensen, J. Bonde, J. H. Nielsen, S. Horch and I. Chorkendorff, *Science*, 2007, **317**, 100–102.

41 J. Xie, J. Zhang, S. Li, F. Grote, X. Zhang, H. Zhang, R. Wang, Y. Lei, B. Pan and Y. Xie, *J. Am. Chem. Soc.*, 2013, **135**, 17881–17888.

42 J. Shi, D. Ma, G.-F. Han, Y. Zhang, Q. Ji, T. Gao, J. Sun, X. Song, C. Li, Y. Zhang, X.-Y. Lang, Y. Zhang and Z. Liu, *ACS Nano*, 2014, **8**, 10196–10204.

43 D. Kong, H. Wang, J. J. Cha, M. Pasta, K. J. Koski, J. Yao and Y. Cui, *Nano Lett.*, 2013, **13**, 1341–1347.

44 H. Tang, K. Dou, C.-C. Kaun, Q. Kuang and S. Yang, *J. Mater. Chem.A*, 2014, **2**, 360–364.

45 G. A. Somorjai, K. R. McCrea and J. Zhu, *Topics in Catalysis* 2002, **18**, 157–166.

Acknowledgements

This work was supported by the National Natural Science Foundation of China (21373196, 11434009), the National Program for Thousand Young Talents of China and the Fundamental Research Funds for the Central Universities (WK2340000050, WK2060140014).

Figures

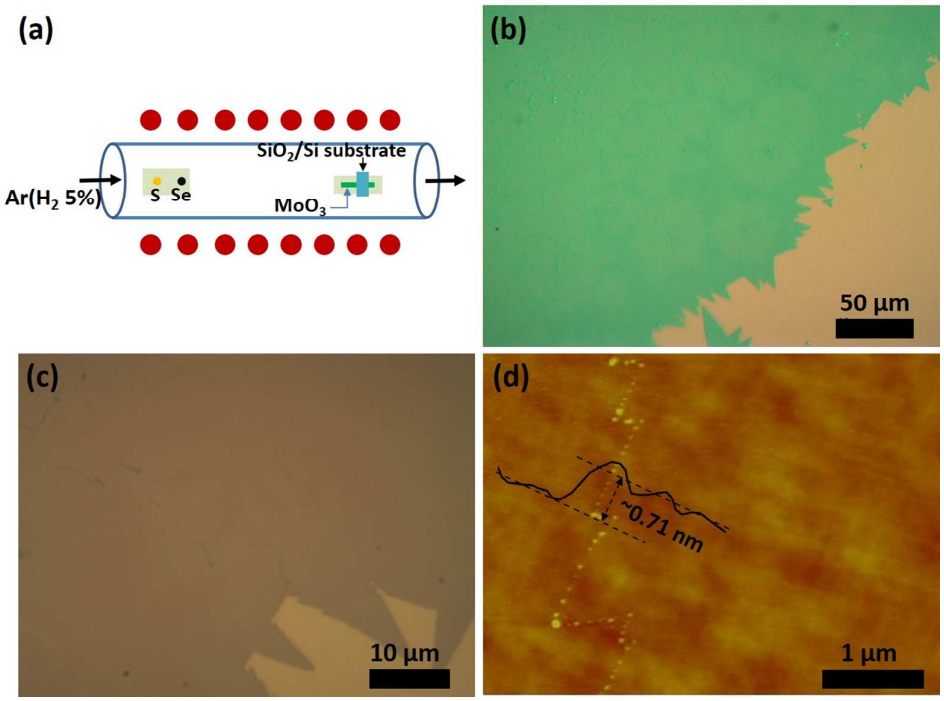

Fig. 1 (a) Schematic illustration for the growth of monolayer $MoS_{2(1-x)}Se_{2x}$ alloy on SiO_2/Si substrate in tube furnace using a CVD method. (b) Low magnification and (c) high magnification OM images of as-grown monolayer $MoS_{1.22}Se_{0.78}$. (d) AFM image of large-area monolayer $MoS_{1.22}Se_{0.78}$ alloy. The height profile presents the $MoS_{1.22}Se_{0.78}$ alloy with a thickness of ~0.71 nm.

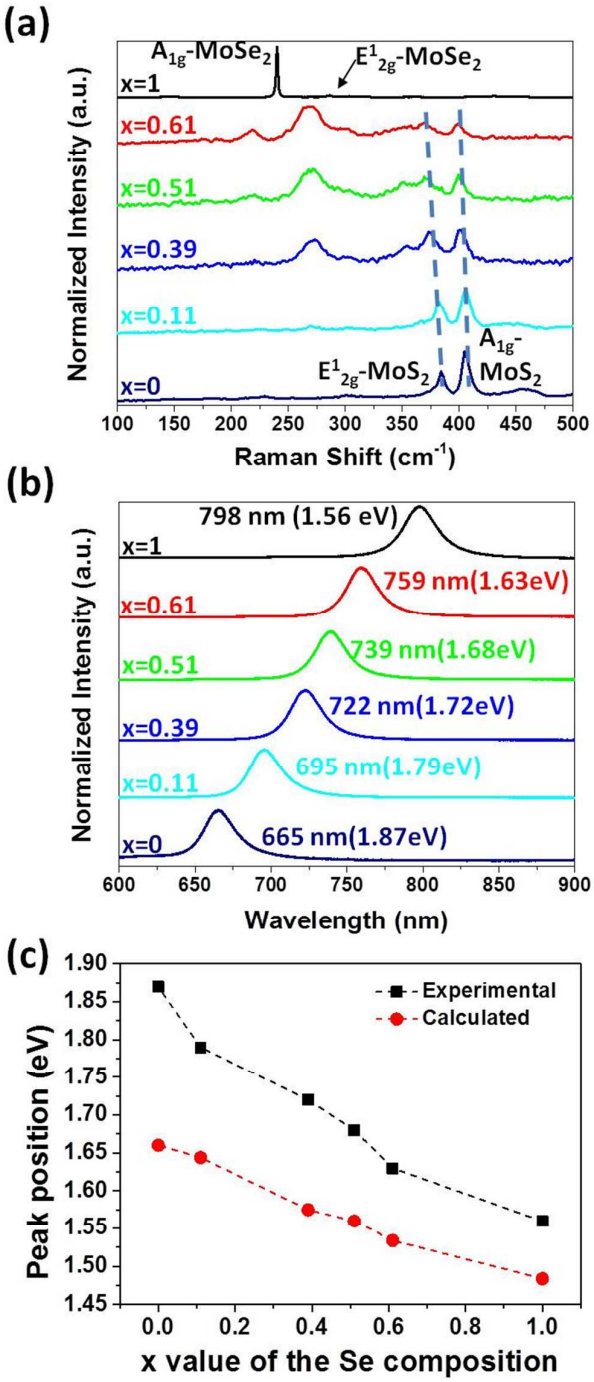

Fig. 2 (a) Raman spectroscopy of as-grown monolayer $MoS_{2(1-x)}Se_{2x}$ alloy with x values of 0, 0.11, 0.39, 0.51, 0.61 and 1. (b) PL spectroscopy of as-grown monolayer $MoS_{2(1-x)}Se_{2x}$ alloy with x values of 0, 0.11, 0.39, 0.51, 0.61 and 1. (c) The bandgap dependence on the Se content in the as-grown monolayer $MoS_{2(1-x)}Se_{2x}$ extracted from (b), consistent with our theoretical calculations (in red).

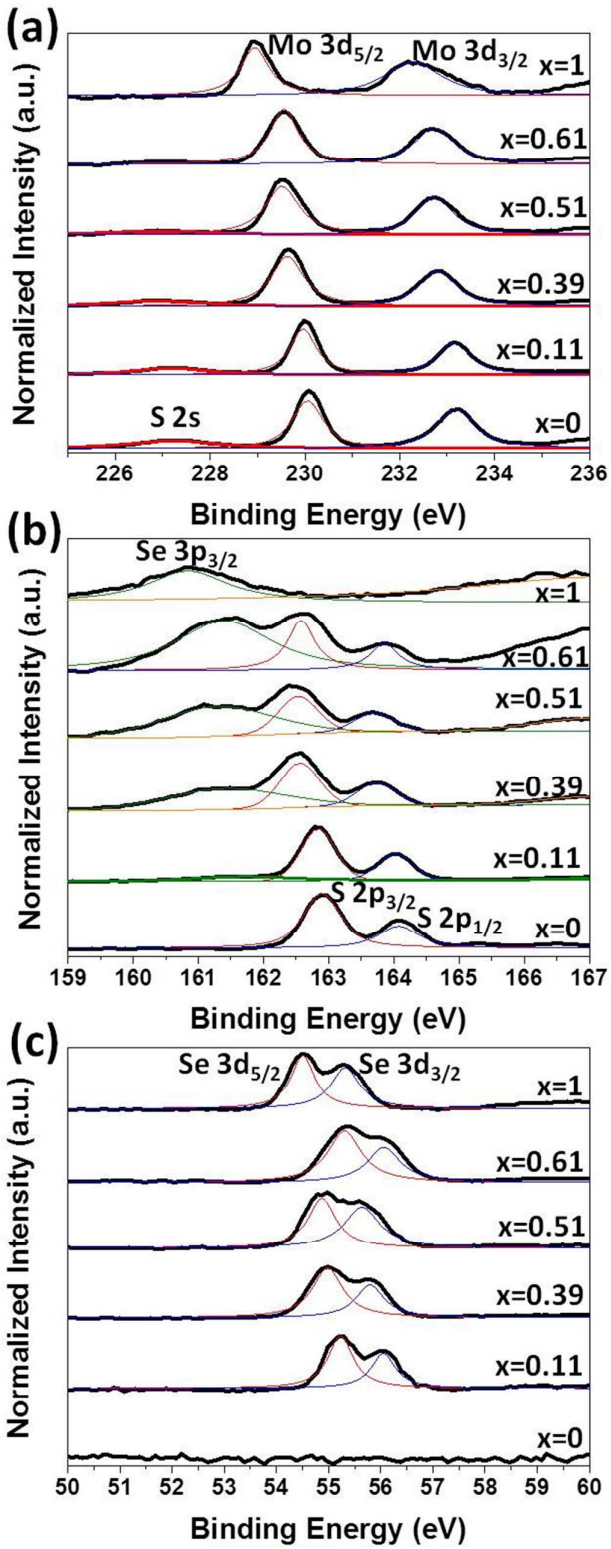

Fig. 3 XPS measurements for Mo, S and Se binding energies with fitted curves in the as-grown monolayer $MoS_{2(1-x)}Se_{2x}$ (x=0, 0.11, 0.39, 0.51, 0.61, 1).

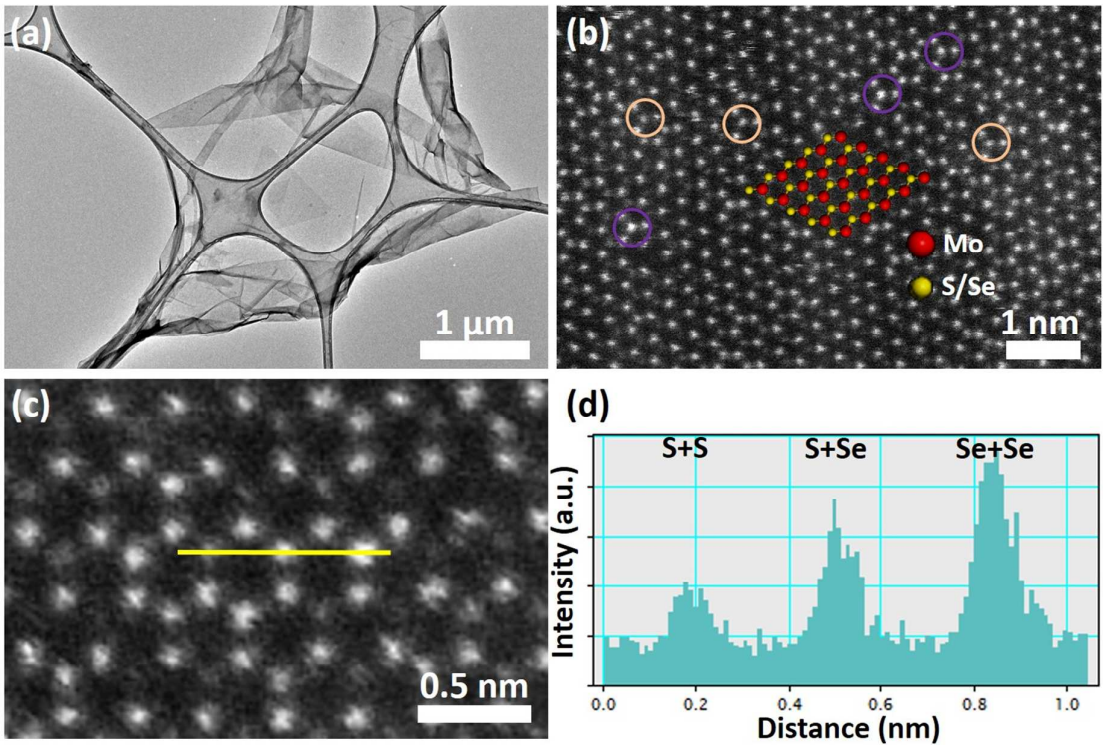

Fig. 4 (a) TEM image of monolayer $MoS_{1.22}Se_{0.78}$. (b) HRSTEM image of monolayer $MoS_{1.22}Se_{0.78}$. The atomic lattice is illustrated by the hexagonal rings of alternating molybdenum and sulfur atoms denoted by the cartoon color spheres. The orange and purple cycles show that the S-S sites are substituted by the single Se atom and two Se atoms, respectively. (c) A higher magnification image of the HRSTEM image in (b). (d) The intensity profiles of the labeled yellow line in (c), which highlights the single- and double-Se substitutions of the S-S sites.

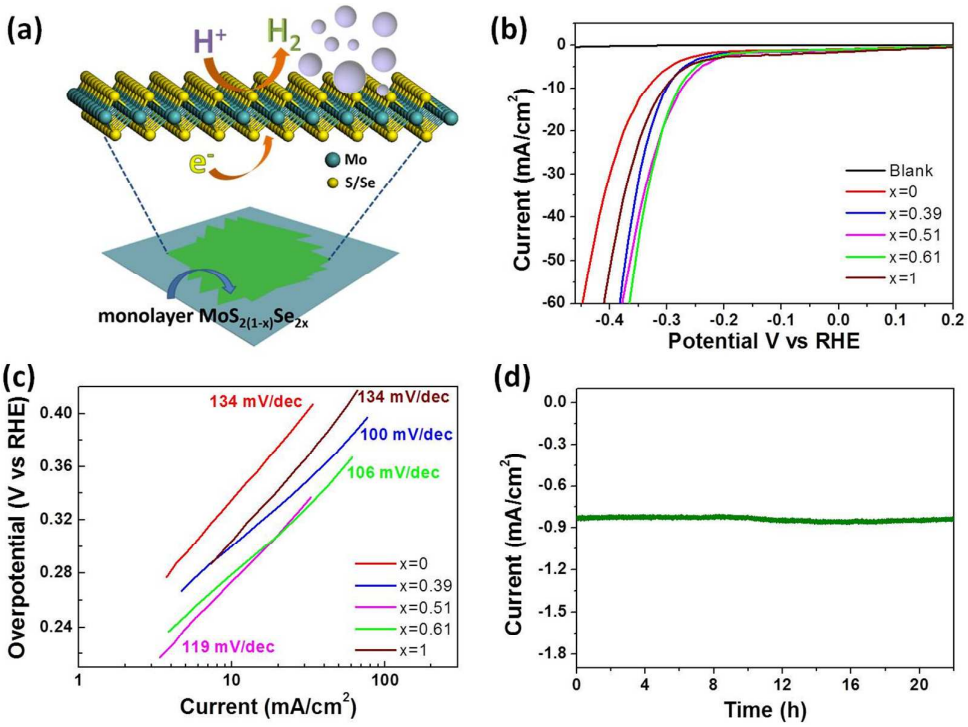

Fig. 5 Electrocatalytic performance of monolayer $MoS_{2(1-x)}Se_{2x}$ alloy on GCE. (a) Schematic illustration of the HER catalytic activity in the monolayer $MoS_{2(1-x)}Se_{2x}$ alloy. (b) Polarization curves of monolayer $MoS_{2(1-x)}Se_{2x}$, and bare GCE. (c) Tafel slopes of monolayer $MoS_{2(1-x)}Se_{2x}$ extracted from the linear part of the polarization curve in (b) and drawn in logarithmic coordinates. (d) Time dependence of the current density under a constant overpotential of -0.24 V for 22 hours in the monolayer $MoS_{2(1-x)}Se_{2x}$ (x=0.61).